Lab on a Chip

PAPER

Oxygenation by a superhydrophobic slip G/L contactor

Elif Karatay and Rob G. H. Lammertink*

The compelling need for an efficient supply of gases into liquids or degassing of fluids within confined microchannels triggered our study on membrane assisted microchemical systems. Porous hydrophobic flat/micro-structured polyvinylidene fluoride (PVDF) membranes were fabricated and integrated in a glass G/L contacting microfluidic device with the aid of optical adhesives. The oxygen transport in microchannels, driven by convection and diffusion, was investigated both experimentally and numerically. The effects of intrinsic membrane morphology on the G/L contacting performance of the resultant membranes were studied. The experimental performance of the flat membranes are shown to obey the simulation results with the assumptions of negligible gas phase and membrane mass transfer limitations. Micro-structured membranes revealed apparent slippage and enhanced mass transport rates, and exceeded the experimental performance of the flat membranes.

1 Introduction

Gassing/degassing of fluids has dozens of applications in (bio)chemical engineering for both reacting and non-reacting processes. Instead of employing conventional direct contacting equipment, such as venturi injectors, wet scrubbers, distillation columns and falling film wall reactors, the use of membranes for contacting has various advantages. These include high interfacial area, hydrodynamic decoupling of different phases, and reduced mass transfer resistance.[1–3] Membrane contactors make important contributions to several useful process intensification methods, such as membrane reactors, absorbers, and degassers.

Porous hydrophobic gas liquid (G/L) contacting membranes have attracted increasing attention and have numerous applications in the removal of acidic gases such as CO_2,[2–4] H_2S,[5,6] or NO_x[7] from exhaust gases, ammonia removal from water,[8] carbonation of soft drinks, blood oxygenation (artificial lungs),[9,10] as well as in heterogeneously catalyzed gas-liquid reactions. This is due to the intense contact of G/L/S phases reducing the mass transfer limitations, separating gaseous and liquid reactants, and hence resulting in higher selectivities at higher conversions.[11,12]

As reported elsewhere,[12–16] the unique properties of microsystems, such as their high surface to volume ratio, short molecular diffusion distance, easy scale up, highly reduced waste, precise control parameters, and the opportunity to integrate unit operations on these micro-scale devices, are among the reasons for the growth in research on microchemical systems. Since the early 2000s, there has been an increasing tendency to utilize membranes for the integration of separation and reaction

University of Twente, Soft Matter, Fluidics and Interfaces, MESA+ Institute for Nanotechnology, Drienerlolaan 5, 7500AE, Enschede, The Netherlands. E-mail: r.g.h.lammertink@utwente.nl; Fax: +31 53 489 2882; Tel: +31 53 489 4798

functionalities to the micro-devices.[10,12–22] Noticeably, PDMS, as an optically transparent, flexible rubbery polymer, that enables gas permeation, is easy to integrate to microdevices and used as a membrane material in many fields. These include analytical, organometallic chemistry, and biology for G/L contacting purposes, specifically, for the delivery of controlled amounts of oxygen in tissue engineering applications,[18–22] as well as in G/L phase photosynthetic oxygenation,[13] and partial oxidation reactions.[12,17] These recent studies highlight the compelling need to ensure an efficient supply of gases into confined liquids in a controlled manner with high accuracy. They reveal room for investigating new polymeric materials in membrane-integrated-microfluidics.

The advent of micro/nano-fluidics has motivated great interest in interfacially driven transport in tiny channels where the bulk fluid motion is realized by convection. Because the hydrodynamic resistance increases with decreasing channel size, avenues for efficient fluid flow at such scales can be addressed. Pressure-driven flow can be enhanced by surfaces that allow hydrodynamic slippage of the fluid on the solid, amplifying the interfacially driven transport phenomena as well. Recent studies concluded that with a smooth hydrophobic surface, one can not reach slip lengths more than a few tens of nanometers unless the surface roughness or topographic structures are specifically engineered.[23] The existence of slip velocity on a porous surface has been verified.[24,25] Slippage on porous materials is connected with the additional G/L interface of relevance to the gas injection/suction at the porous wall. These considerations imply the potential of new porous materials that can be fabricated and topographically structured with simple methods in microfluidics. These porous materials can contribute significantly to hydrodynamic slippage and hence to the improvement of interfacial phenomena, including gas transport to or from the confined microchannels.

PVDF is a very promising membrane contactor material due to its hydrophobicity and excellent chemical resistance, particularly towards oxidation. Its solubility in organic solvents allows facile fabrication compared to other hydrophobic polymers such as polypropylene (PP), polyethylene (PE) and polytetrafluoroethylene (PTFE). Porous PVDF membranes are frequently used in membrane science for numerous applications,[2–8] and in establishing intimate contact of G/L/S interfaces for heterogeneously catalyzed multi-phase reactions.[11] PVDF is also of interest in Bio-MEMS for sensing and actuation applications due to its biocompatibility and stable piezoelectric impedance properties.[26,27] The superior characteristics of PVDF make it prone to a broad range of new applications in microchemical systems.

Direct bonding, such as anodic bonding, plasma bonding or fusion bonding, is one of the most used methods in the field of microfluidics. However, the applicability of this method is limited by the type of material from which the chip components are produced. It can be further limited by harsh conditions (high temperature, oxidative plasma, high voltage) that can be destructive for the characteristic properties of the chip components. These considerations become critical when one of the chip components is polymeric. Apart from direct methods, bonding techniques by means of gluing two components of the chip were reported to be effective at milder conditions.[28–30] A wide range of materials, including epoxy glue,[31] Hysol,[32] SU-8,[33] parylene,[34] polyimide,[28] PDMS,[35] and UV-curable adhesives,[30] were among the materials applied as an intermediate layer for bonding LOC substrates.

In the present study porous micro-structured super-hydrophobic PVDF membranes are integrated into fluidic glass chips by means of UV curable adhesives. The mass transfer efficiency of the proposed microdevice is tested by oxygen saturation experiments. The experimental results are verified by numerical modeling.

2 Materials & methods

2.1 Experimental

2.1.1 Glass chips. Meander microchannels for liquid flow and micro-reservoir for gas flow were fabricated by standard photolithography followed by chemical (HF) wet etching on separate borofloat glass wafers. The wafers were diced to obtain glass chips with dimensions of 2 cm x 1.5 cm. The channel width and channel height of the meandering channels were varied in the range of 300–500 μm and 50–100 μm, respectively. The length of the micro-channel was 13.5 cm. The micro-reservoirs for gas flow have dimensions of 1.2 cm × 1.5 cm with a depth of 50 μm.

2.1.2 Membranes. PVDF membranes were prepared by the immersion precipitation method.[36] 20 wt% PVDF (Solvay, Solef) is dissolved in dimethyl acetamide (DMAc, Merck) by magnetic stirring at 65 °C overnight. The polymer solution was cast at a thickness of 600 μm on a silicon wafer by an automatic film applicator. The polymeric films were phase separated in three different non-solvents: water, ethanol, and a water/ethanol (50/50 v%) mixture. The polymeric film was placed in the

coagulation medium for 2 h, after which the coagulation bath was replaced with fresh non-solvent. The film was kept in this coagulation medium for 24 h. The film was put in three consecutive ethanol (Assink Chemie) baths, followed by three consecutive n-hexane (Merck) baths. After the films were dried, they were kept in a vacuum oven at 30 °C. Micro-structured PVDF membranes containing pillars with a diameter of 10 μm and an aspect ratio in the range of 1–4 were prepared by phase separation micro molding.[37] Wafers containing holes with diameters of 10 μm, separation distance of 10 μm, and with depths of approximately 13 μm and 35 μm were prepared by SU-8 patterning. The polymer solution was cast on these wafers, hence the replica of the micro-structure pattern was obtained on the membranes. The morphology of the fabricated membranes was characterized by SEM (JEOL JSM 5600LV). Apparent porosity measurements were done with a pycnometer (Micromeritics, Accupyc 1330). N_2 permeance experiments were performed using a capillary flow porometer (Porolux-1000) at 1 bar. The hydrophobicity of the membranes was tested by contact angle measurements (Dataphysics, OCA 20). The membranes were further characterized by clean water breakthrough pressure experiments. Flat, dense PDMS membranes with a thickness of 100 μm were prepared by casting prepolymer (Permacol B. V., RTV-A) and a crosslinking agent (Permacol B. V., RTV-B) on a silicone wafer, followed by curing for one day at 60 °C. The ratio of prepolymer to crosslinking agent was 10 : 1, and the mixture was degassed before casting.

2.1.3 Chip assembly. UV-curable adhesives were employed to bond porous hydrophobic PVDF membranes to glass substrates. Among the different types available in the market, selection was performed for the specific polymer substrate of interest by considering the viscosity, composition, and the solvents used in the formulation of the glue, which all affect the adhesion due to the hydrophobic nature of the membranes. NOA 78 (Norland Optical Adhesive) showed satisfactory adhesion, and was selected as the gluing material between glass and PVDF membranes. The methodology reported by Arayanarakool et al.[30] was employed. The glass chips were cleaned in an O_2 plasma cleaner (Harrick Plasma) for 10 min before bonding. The optical adhesive was spin coated on a blank glass plate at 2000 rpm for 90 s. A thin layer of uncured glue was transferred to the structured glass substrate (either including the meander channels or the gas sink) by means of a roller. Once the uncured glue was conveyed to the glass chips, the membrane was aligned such that the effective G/L contacting spots were not contaminated with the adhesive. Once the glass-membrane-glass assembly was cured by UV exposure for 10 min, it was inserted into a custom made chip holder, as shown in Fig. 1a.

2.1.4 Experiments and set-up. A syringe pump (HARVARD Apparatus PHD 2000) was used to control the flow rate of liquid in the glass micro-channels. De-oxygenated water was used as liquid feed. Pure oxygen was fed to the micro-reservoir from the opposite side of the assembly. For the oxygen flow through the gas sink on the glass chip, either the flow rate of the gas (1 ml min^{-1}) was controlled by a mass flow controller (BRONKHORST, El-Flow), or the pressure of the gas (0–2 bar) was controlled by a pressure reducer. In the multilayer
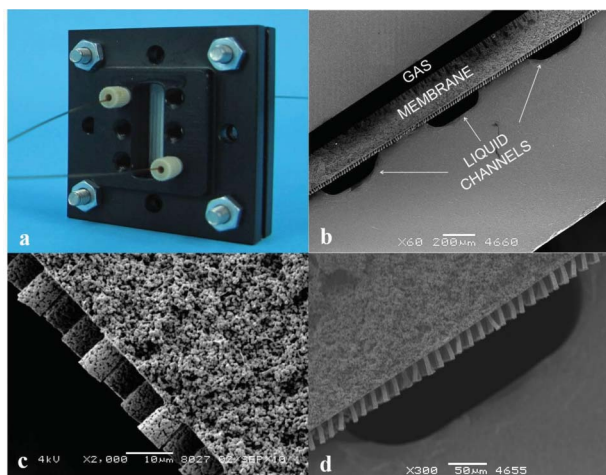
Fig. 1 G/L contacting micro-device: a) Optical image of PVDF membrane integrated micro-device with fluidic connections. b) Cross sectional SEM image of the gas sink-micro-structured membrane-liquid microchannel assembly at a magnification of 60×. c) Cross sectional SEM image of a microstructured membrane with short pillars. d) Cross sectional SEM image of the gas sink-micro-structured membrane-liquid microchannel assembly at a higher magnification of 300×.

glass-membrane-glass assembly, the gas diffuses through the membrane to the liquid channel. The dissolved oxygen content of the outlet liquid was measured by a fiber optic oxygen sensor (FIBOX 3, PreSens). The experimental dissolved oxygen concentration data was recorded. The liquid flow rate was varied in the range of 25 μl min^{-1} to 2 ml min^{-1} while the gas flow rate and/or pressure was kept constant during the experiments.

2.2 Numerical analysis

The oxygen concentration profile evolution in the microchannels was numerically studied. 2D and 3D models were solved by finite element methods using COMSOL Multiphysics 4.1 software. The subdomain mesh consisted of 1936 and 1314593 elements for the 2D and 3D cases, respectively. The geometry of the meander channels on home-made glass chips was used in 3D analysis, whereas a simplified straight channel geometry was used in 2D analysis. The Navier–Stokes equation for hydrodynamics was coupled with convection-diffusion equation for the mass transport and solved for the liquid side with an assumption of non-wetted membrane pores, hence neglecting mass transfer resistance across the porous membrane. Assuming the G/L interface is established at the liquid side of the membrane, the interface oxygen concentration (C_i) can be related to the partial pressure (p_i) of the gas at the interface by Henry's law;

$$C_i = \frac{p_i}{H} \tag{1}$$

where $H = 7.67 \times 10^7$ Pa (mol l^{-1})$^{-1}$ is Henry's coefficient for O$_2$ in water.[38] With physical adsorption at these conditions and a constant interface concentration at the porous PVDF membrane boundary of the liquid side microchannels, mass transfer can be described by;

$$V_y(x)\frac{dC}{dy} = D\frac{d^2 C}{dx^2} \tag{2}$$

where D is the oxygen diffusion coefficient in water ($D = 1.97 \times 10^{-9}$ m^2 s^{-1}),[38] and $V_y(x)$ is the velocity of the longitudinal bulk flow. The inlet boundary condition to the microchannel was set at zero. In three dimensional analysis, the Navier–Stokes equation was numerically solved. In two dimensional analysis, the Hagen–Poiseulle slit analog velocity profile was imposed eqn (3). A schematic illustration of the 2D model geometry and the mass transfer boundary conditions is represented in Fig. 2c.
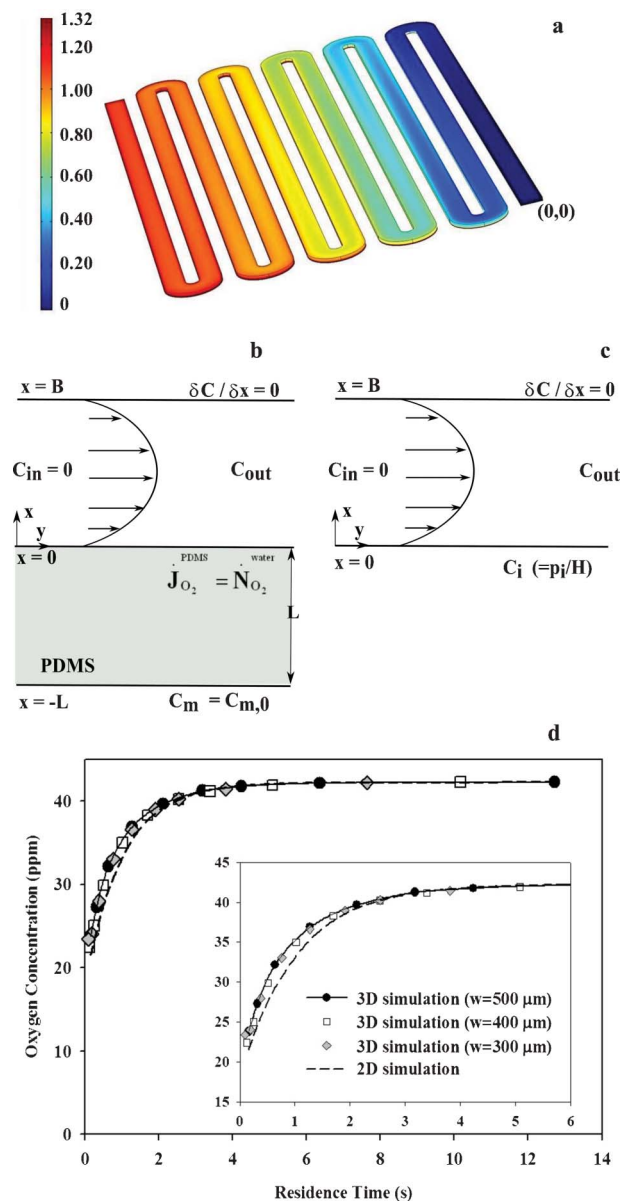

Fig. 2 Numerical analysis: 3D surface plot of oxygen concentration profile in the 500 μm wide, 100 μm deep meander microchannel (a). Illustration of 2D model geometry regarding assemblies with PDMS membrane (b) and with porous PVDF membranes (c). The effect of varying microchannel widths for 3D simulation, and the comparison of 2D and 3D simulations on the average outlet oxygen concentration with respect to varying liquid residence time (d).

$$V_y(x) = 4V_{\max}\frac{x}{B}\left(1 - \frac{x}{B}\right) \qquad (3)$$

The average O_2 concentration at the outlet of the liquid side microchannel was determined by boundary integration over the normal outflow;

$$<C> = \frac{\int CV_y(x)\mathrm{d}x}{\int V_y(x)\mathrm{d}x} \qquad (4)$$

Numerical analysis was also performed for oxygenation using a PDMS membrane, including the thickness of the dense PDMS membrane, for comparison purposes. Additional mass transfer resistance offered by the gas diffusion across the PDMS membrane and the boundary conditions are described in eqn (5)–(7).

$$D_m\frac{\mathrm{d}^2 C_m}{\mathrm{d}x^2} = 0 \qquad (5)$$

$$x = -L,\ C_m = C_{m,0} \qquad (6)$$

$$x = 0, \qquad D_m\frac{\mathrm{d}C_m}{\mathrm{d}x} = \dot{N}_{O_2}^{\text{water}} \qquad (7)$$

C_m is the concentration of oxygen in the membrane phase. $C_{m,0}$ is the adsorbed oxygen concentration at $x = -L$, where PDMS membrane contacts pure oxygen gas phase at 1 bar and 25 °C. $C_{m,0}$ is expressed in terms of the oxygen partition coefficient in PDMS ($K_g = 0.3$) and the concentration of oxygen in the gas phase ($C_{g,b} = 40$ mol m^{-3}) to be $K_g C_{g,b}$. Similarly, $C_{m,L}$, the desorbed oxygen concentration at $x = 0$, where PDMS membrane contacts water flow in the microchannel, is expressed in terms of oxygen partition coefficient in water ($K_w = 10$) and local concentration of oxygen in the liquid phase (C) to be $K_w C$. The oxygen flux across the PDMS slab equals the oxygen flux to water ($\dot{N}_{O_2}^{\text{water}}$) at $x = 0$, and eqn (7) becomes;

$$x = 0, \qquad D_m\frac{K_g C_{g,b} - K_w C}{L} = \dot{N}_{O_2}^{\text{water}} \qquad (8)$$

For the liquid phase, the Hagen–Poiseulle slit analog velocity profile eqn (3) is used for longitudinal bulk flow, and the differential mass balance describing the oxygen concentration profile in the liquid eqn (2) is numerically solved using the flux boundary condition represented in eqn (8). A schematic illustration of 2D model geometry including the PDMS membrane and the corresponding mass transfer boundary conditions are represented in Fig. 2b.

3 Results and discussion

3.1 Numerical simulations

2D and 3D models governing the momentum and mass transfer in the liquid channels were solved with the assumptions of no slip

velocity at the channel boundaries and O_2 saturated liquid at the membrane boundary, neglecting mass transfer resistance across the porous membrane. Fig. 2a represents the 3D model geometry and the steady state dissolved oxygen concentration profile in a meander microchannel with a width of 500 μm and a height of 100 μm for a water flow rate of 250 μl min^{-1} and a Reynolds number of 10.6. As the surface plot illustrates, de-oxygenated water is saturated along the channel as O_2 diffuses from the membrane to the water. The bottom surface boundary is prescribed to the solubility value of pure oxygen in water at 273 K and 1 bar (1.32 mol m^{-3}).

The mass transfer behavior of the liquid side with varying channel width (300–500 μm) was investigated and compared with 2D simulations for different liquid residence times (Fig. 2d). The residence time of the liquid in the microchannel was calculated from the ratio of channel volume to flow rate. The volumes of 300, 400, and 500 μm wide channels are 3.2, 4.2, and 5.3 μl respectively. As Fig. 2d presents, the O_2 transport is hardly influenced by the width of the liquid channel in this range. Furthermore, the two dimensional analysis, which is equivalent to a parallel plate configuration, agrees with the three dimensional analysis. The slight deviations at higher flow rates can be attributed to the so-called race track affect at the corner of the meandering channels in 3D geometry.

The numerical results presented should show the fastest oxygen saturation possible, since the mass transfer limitations on the gas side and on the membrane side are neglected. Only the mass transfer limitation in the liquid phase is taken into account as the G/L interface is situated at the liquid side of the membrane.

3.2 Membrane characterization

Immersion precipitation is a phase separation process that includes the exchange of the solvent in the thin polymer film by the non-solvent in the coagulation bath. 20 wt% PVDF/DMAc films were phase separated in three different coagulation mediums: water (M2), ethanol (M3), and water/ethanol (50/50 v%) (M1). The apparent porosity values of the prepared membranes, tabulated in Table 1, are comparable to a commercially available, hydrophobic membrane (Accurel® PP 2E HF, MEMBRANA). The N_2 permeance results and the breakthrough pressure values of these membranes are also tabulated in Table 1. As indicated by the gas permeation and breakthrough pressure values, the coagulation medium in which the membrane was formed influences the internal membrane structure. The membrane that was phase separated in water (M2) showed 100 times less permeance compared to the membrane

Table 1 Internal characteristics of home made membranes in comparison to commercial membrane

Membrane	Porosity (%)	N_2 Permeance (GPU [a])	P_b (bar)
Accurel®	80	3.68×10^5	2.2
M1[b]	75	5.36×10^5	2.6
M2[c]	75	0.17×10^5	3.5
M3[d]	77	13.10×10^5	1.1

[a] 1 GPU = 10^{-6} cm^3/cm^{-2} s^{-1} cm Hg^{-1}. [b] Phase separated in water/ethanol (50/50 v%). [c] Phase separated in water. [d] Phase separated in ethanol.

that was phase separated in ethanol (M3), even though the apparent porosity values of these membranes are approximately the same. The membrane that was phase separated in the water/ethanol mixture (M1) has a N_2 permeance value in between M2 and M3, and was comparable to the commercial membrane.

These findings indicate the effect of the coagulation medium on the surface porosity of the prepared membranes. The use of different non-solvents alters the rate of polymer precipitation. Likewise, the breakthrough pressure values of the prepared membranes are in agreement with the sequence of increasing effective porosity: M3 > M1 > M2.

In micro scaled systems, porous materials have numerous benefits. In particular for gassing/degassing applications, where an additional layer is used to decouple the gas and liquid flow. Porosity can play a significant role by determining the mass transfer rate limiting step. The use of PDMS, being highly permeable material to gases and vapors, has been acknowledged in bio-microfluidics by several authors.[18–22] The gases permeate by a solution-diffusion mechanism in the dense PDMS films. The gaseous oxygen molecules are incorporated in the PDMS membrane by preferential sorption. The adsorbed oxygen diffuses across the PDMS film and is desorbed at the other side, partitioning in the water phase. This mode of oxygen transport across the membrane offers an additional mass transfer resistance proportional to film thickness. Using the literature N_2 permeability value,[39] the N_2 permeance of a PDMS film with a thickness of 100 μm can be calculated to be 2.8 GPU, which is 5 orders of magnitude smaller than the N_2 permeance values of the porous PVDF membranes presented in Table 1. The pore sizes of the presented membranes are larger than the mean free path of the gas molecules, hence the transport limitation is negligible compared to dense membranes. In addition to mass transfer resistance, non-porous membranes show a selectivity over different gases. The O_2/N_2 and CO_2/N_2 selectivity values for PDMS are reported to be 2 and 12, respectively.[39] Therefore, the transport rate of these gases through PDMS films are different, which could be critical for the applications in cell culture environments, or Bio-MEMS related sensors and actuators for which the exchange rate of those gases can be essential. The use of porous membranes in gas liquid contactors eliminates the size/affinity discrimination of the permeating gas molecules.

Table 2 presents the results of dynamic contact angle measurements. A flat porous PVDF membrane was pressed at 50 °C and 2 ton in a Hydraulic Press (Specac) to obtain a dense PVDF film (M0). The advancing contact angle of this smooth, dense PVDF film was measured to be 83° ± 2, with a large hysteresis of 23°. The flat, phase separated membrane (M1) showed an increased advancing contact angle, with a smaller

Table 2 Contact angle measurements of flat/micro-structured membranes phase separated in water/ethanol (50/50 v%) in comparison to a dense PVDF film

Membrane	Advancing CA (°)	Receding CA (°)	Hysteresis
M0[a]	83	57	26
M1[b]	159	146	13
M4[c]	165	158	7
M5[d]	164	158	6

[a] Dense PVDF film. [b] Flat PVDF membrane. [c] PVDF membrane with short pillars. [d] PVDF membrane with tall pillars.

hysteresis value due to surface roughness. Contact angle values of micro-structured membranes M4, PVDF membranes with short pillars (Fig. 1c) and M5, PVDF membranes with tall pillars (Fig. 1d) were further improved to values above 160°, with considerably diminished hysteresis. These observations are indicative of a Cassie–Baxter state of topographically engineered M4 and M5 membranes. In this state, the liquid rests on the tops of micro-structures.

Hydrophobic materials that can prevent wetting are used to minimize the mass transfer limitations. Due to the hydrophobic nature of PVDF polymers and the surface roughness obtained by the phase separation technique, M1 membranes revealed an improved hydrophobicity. The micro-structured membranes (M4 and M5) showed superhydrophobic behavior owing to the combination of surface roughness/porosity and micro-pillars. These findings are in agreement with previous studies that investigated composite G/L/S interfaces on micro-patterned surfaces,[40–42] and imply the possibility of obtaining a Cassie–Baxter state on the prepared micro-structured membranes.

3.3 Gas transport

The oxygen contacting performance of the porous flat/micro-structured hydrophobic/superhydrophobic PVDF membranes was tested. Oxygen diffuses across the membrane, and a G/L interface is established at the membrane boundary of the liquid channel. Dissolved oxygen evolving from the membrane boundary is convectively transported by the initially deoxygenated water flow along the channel.

Fig. 3a shows the influence of variation in the liquid flow rate on the oxygen uptake for different membranes in comparison to the simulation results. For all of the membranes presented, larger residence times, and hence lower water flow rates, lead to higher outlet oxygen concentrations. According to the model predic-
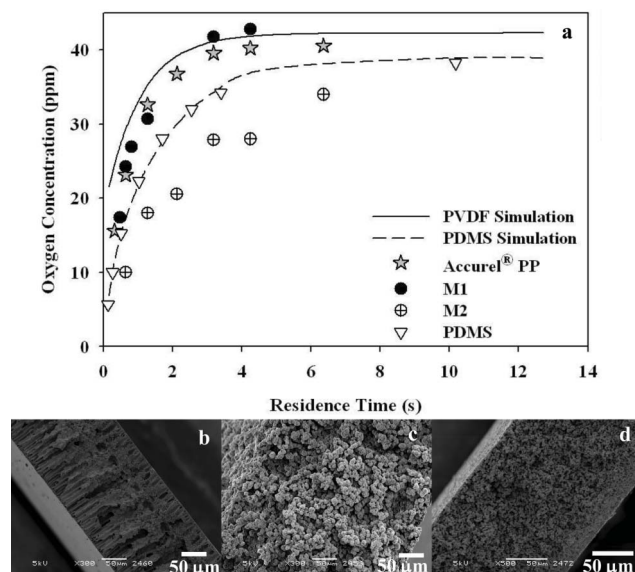

Fig. 3 Effect of internal membrane structure. O_2 absorption behavior of different membranes with respect to liquid residence time for a 500 μm wide, 100 μm deep channel (a). Cross sectional SEM images of 20 wt% PVDF membranes that were coagulated in water (b), in ethanol (c), and in water/ethanol (50/50 v%) (d).

tions, the oxygen concentration varies abruptly in the first 2 s, and the channel (500 μm wide, 100 μm deep) is fully saturated within 3 s at the utmost. The home-made PVDF membrane that was phase separated in a water/ethanol (50/50 v%) mixture (M1) and the commercial membrane are in good agreement with the model predictions. Fig. 3a illustrates the oxygen uptake results for the membrane that was phase separated in water (M2) at a gas pressure of 2 bar. The slower response and gas side pressure dependency of the membranes coagulated in water reveals an additional mass transfer resistance in the membrane side for oxygen diffusion. The additional mass transfer limitation for the M2 membrane may stem from wetting of the membrane pores or from the particular morphology of the membrane. A closed pore structure increases the mass transfer resistance to O_2 diffusion across the membrane.

Fig. 3b–d shows the cross sectional SEM images of the M1, M2, and M3 membranes. It is apparent from Fig. 3b that the use of water as a coagulant results in an asymmetric morphology with finger-like macrovoids and a dense skin layer. The use of ethanol as the coagulant results in a uniform morphology consisting of spherulites (Fig. 3c). The morphology of the resultant membranes indicates that water acts as a strong non-solvent, which results in a dense skin layer, while ethanol acts as a milder non-solvent that introduces a delay time for L/L demixing, in agreement with literature findings.[36,43,44] Hence, the slower G/L contacting response and the lower N_2 permeance value (Table 1) of M2 can be attributed to the formation of a denser layer, resulting in gas phase mass transfer resistance to O_2 diffusion across the membrane.

Gas liquid contacting experiments on membranes produced with ethanol as a coagulant were also conducted. However, liquid cross over to the gas side was observed for flow rates larger than 400 μl min^{-1}. Fig. 3d illustrates the morphology of M1. Addition of ethanol eliminated the formation of macrovoids, and the skinned asymmetric structure of phase separated membranes with pure water. Using the water/ethanol (50/50 v%) mixture as a coagulant results in successful gas/liquid contacting membranes, verifying the numerical simulations that were solved for the non-wetted mode of operation. These findings and the O_2 transfer experiments clearly indicate the influence of membrane morphology on the G/L contacting performance of the resultant membranes, and the opportunity of tuning porosity introduced in the micro-contactor. Moreover, the results of M1 membranes show that the major mass transfer resistance for O_2 transport is in the liquid phase. The G/L contacting interfaces formed at surface pores of the membrane decreases the hydrodynamic resistance in the confined microchannel.

The gas liquid contacting performance of chip assembly including a flat, dense PDMS membrane with a thickness of 100 μm is illustrated in Fig. 3a, in comparison to porous PVDF. In accordance with the PDMS simulation results, where the additional mass transfer resistance to O_2 diffusion across the PDMS membrane is included, the gas uptake is lower once the PDMS membrane is employed. Moreover, this major mass transfer resistance across the PDMS membrane retards the saturation of the microchannel such that an average outlet O_2 concentration of 39 ppm can be reached at utmost. The microchannel is fully saturated within 3 s when the porous PVDF membranes are employed. The use of porous PVDF

membranes can eliminate thickness dependent membrane side mass transfer resistance. In addition, they reduce the residence time required for full O_2 saturation, and eliminate undesired size/affinity gas selectivity.

To investigate the mass transfer behavior on the liquid side, O_2 saturation experiments were performed for various water flow rates in 400 μm wide channels with depths of 50 and 100 μm. The oxygen concentration at the channel outlets are plotted with respect to the intrinsic residence time of each channel depth (Fig. 4). The results reveal that the saturation value of oxygen is reached faster for lower channel depth. Shorter diffusion distance in 50 μm deep channel results in faster saturation of the microchannel. Theory predicts that the diffusion time of dissolved oxygen across microchannel cross section is proportional to the square of the channel height, $H \sim \sqrt{2Dt}$, where D is the oxygen diffusivity in water. Fig. 4 shows that the residence time required for full oxygen saturation across the outlet cross section of the microchannels are scaled with the square of channel height. The experimental findings showed that a residence time of approximately 0.6 and 2.5 s is sufficient for oxygen saturation of 50 μm and 100 μm deep channels, respectively, validating the dominant mass transfer resistance is in the liquid phase.

The G/L contacting performance of the assemblies with microstructured membranes were tested. PVDF membranes with shorter (M4) and taller (M5) micro-pillars were used. Fig. 5 shows the oxygen uptake measured at the water channel outlet for membranes M4 and M5 with respect to different residence times in comparison to the flat M1 membrane. Once the microstructured membranes are employed, gas uptake in the microchannel is even faster compared to flat membranes. This enhancement in the mass transport, which is driven by convection-diffusion, may suggest improved hydrodynamics. The superhydrophobicity of the microstructured membranes (Table 2), and the additional gas pockets in between the micro-pillars can induce slip flow at the membrane boundary of the microchannel, which promotes the mass transfer rate of oxygen.

From a practical viewpoint, wall slip can be desirable because of reduction in flow resistance. Hydrodynamic slip can significantly enhance transport phenomena originating at interfaces. Beavers et al.[24] were the first to investigate the fluid flow at
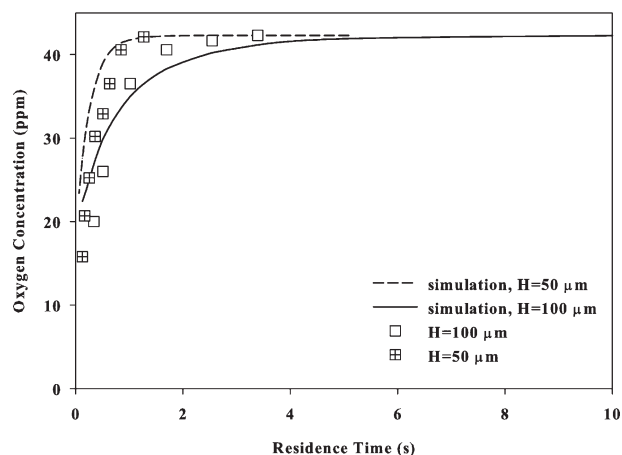

Fig. 4 Outlet oxygen concentrations in change with residence time of the deoxygenated water for different channel depths (width = 500 μm).
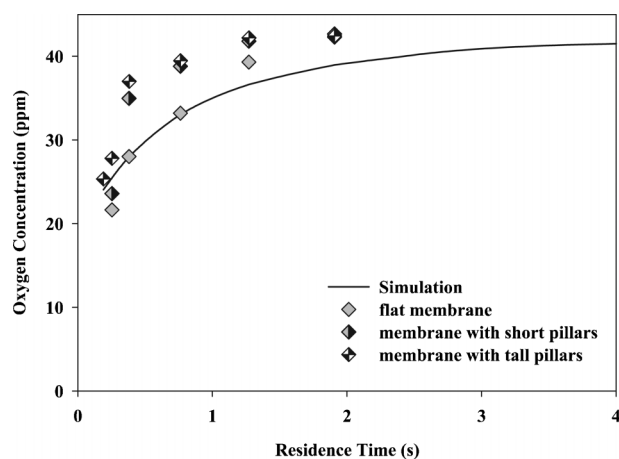
Fig. 5 Influence of using micro-structured membranes on the oxygen mass transfer rate (width = 300 μm, height = 100 μm).

the interface between a porous medium and a fluid layer and proposed a slip boundary condition at the porous interface. Recent reports suggest rough, topographically and chemically heterogeneous, specifically engineered surfaces for generating slip velocity.[23,40–42] Previous studies[40–42] also indicate that the Cassie–Baxter state promotes slippage at the G/L interface in between the micro-pillars. Micro-structuring the PVDF membranes increases the slip effects with additional gas entrapment at the fluid boundary. The amplified mass transport rates demonstrated in Fig. 5 can be attributed to the realization of the Cassie–Baxter state and slippage at the G/L/S boundary owing to the porous micro-pillars. The enhancements of the oxygen uptake for the flow rates 250, 500, and 750 μl min^{-1} are 14%, 20%, and 8% for the microstructured membrane with shorter pillars (M4) and 16%, 28%, and 22% for the microstructured membrane with taller pillars (M5), respectively. The decreased impact of micro-pillars at a flow rate of 750 μl min^{-1} may imply the transition from the Cassie–Baxter to a Wenzel state at higher pressures.

The enhanced mass transfer properties and promoted slippage make these superhydrophobic PVDF membranes suitable for various applications. The intrinsic tunable surface porosity enables the efficient supply and removal of gases for cells. The opportunity of generating shear-free boundaries at the G/L menisci in between the micro-pillars allows their use as porous supports and/or as scaffolds for cells. The superhydrophobicity enables efficient water management. These promising properties of biocompatible, chemically resistant PVDF membranes affirm their high potential in many bio- related microfluidics, Bio-MEMS, tissue engineering, and cell culturing studies.

4 Conclusions

Porous superhydrophobic PVDF membranes were integrated with microfluidic glass chips by the use of UV-curable adhesives. Microfluidic devices comprised of porous hydrophobic polymeric membranes and a conventional LOC substrate, glass, were stacked and sealed in a short time at ambient conditions. The developed assembly technique eliminated the necessity of mechanical compression in order to obtain a leak-free assembly, which in turn prevents any mechanical deformation of the membrane.

Oxygen transport experiments were verified by numerical simulations of the proposed multiple layer micro G/L contactor, and they showed:

1) The membrane morphology, and hence membrane preparation parameters have an influence on the G/L contacting performance of the resultant membranes.

2) An opportunity for the efficient supply of gases into liquids in a controlled manner.

3) The micro-structured membranes further enhance the mass transfer efficiency, as shear-reduced spots are generated at G/L interfaces between the micro-structures, promoting apparent slippage.

The promising properties of the reported porous superhydrophobic PVDF membranes that enhance all manifestations of interfacially driven phenomena confirms their high potential in various applications, particularly for bio-related microfluidics and Bio-MEMS applications.

Acknowledgements

References

1 *Membrane Separations Technology: Principles and Applications*, ed. R. D. Noble and S. A. Stern, Elsevier Science B.V., Amsterdam, 1st edn, 1995.
2 S. Rajabzadeh, S. Yoshimoto, M. Teramoto, M. Al-Marzouqi and H. Matsuyama, *Sep. Purif. Technol.*, 2009, **69**, 210–220.
3 J.-L. Li and B.-H. Chen, *Sep. Purif. Technol.*, 2005, **41**, 109–122.
4 A. Mansourizadeh, A. Ismail and T. Matsuura, *J. Membr. Sci.*, 2010, **353**, 192–200.
5 D. Wang, W. Teo and K. Li, *Sep. Purif. Technol.*, 2004, **35**, 125–131.
6 D. Wang, W. Teo and K. Li, *Sep. Purif. Technol.*, 2002, **27**, 33–40.
7 H. H. Park, B. R. Deshwal, H. D. Jo, W. K. Choi, I. W. Kim and H. K. Lee, *Desalination*, 2009, **243**, 52–64.
8 X. Tan, S. Tan, W. Teo and K. Li, *J. Membr. Sci.*, 2006, **271**, 59–68.
9 A. Gabelman and S.-T. Hwang, *J. Membr. Sci.*, 1999, **159**, 61–106.
10 J. de Jong, P.W. Verheijden, R. G. H. Lammertink and M. Wessling, *Anal. Chem.*, 2008, **80**, 3190–3197.
11 M. G. Buonomenna, E. Drioli, R. Bertoncello, L. Milanese, L. J. Prins, P. Scrimin and G. Licini, *J. Catal.*, 2006, **238**, 221–231.
12 A. Schuster, R. Lakshmanan, J. Ponton and K. Sefiane, *J. Chem. Technol. Biotechnol.*, 2003, **78**, 342–346.
13 C. P. Park, R. A. Maurya, J. H. Lee and D. P. Kim, *Lab Chip*, 2011, **11**, 1941–1945.
14 *Handbook of Micro Reactors*, ed. V. Hessel, J. C. Schouten, A. Renken, Y. Wang and J. I. Yoshida, Wiley-VCH, Weinhem, 2009.
15 *Chemical Micro Process Engineering*, ed. V. Hessel, S. Hardt and H. Löwe, Wiley-VCH, Weinhem, 2004.
16 J. de Jong, R. G. H. Lammertink and M. Wessling, *Lab Chip*, 2006, **6**, 1125–1139.
17 C. P. Park and D.-P. Kim, *J. Am. Chem. Soc.*, 2010, **132**, 10102–10106.
18 M. Polinkovsky, E. Gutierrez, A. Levchenko and A. Groisman, *Lab Chip*, 2009, **9**, 1073–1084.
19 M. Adler, M. Polinkovsky, E. Gutierrez and A. Groisman, *Lab Chip*, 2010, **10**, 388–391.
20 M. Skolimowski, M. W. Nielsen, J. Emneus, S. Molin, R. Taboryski, C. Sternberg, M. Dufva and O. Geschke, *Lab Chip*, 2010, **10**, 2162–2169.
21 J. Park, T. Bansal, M. Pinelis and M. M. Maharbiz, *Lab Chip*, 2006, **6**, 611–622.
22 A. P. Vollmer, R. F. Probstein, R. Gilbert and T. Thorsen, *Lab Chip*, 2005, **5**, 1059–1066.

23 A. Ajdari and L. Bocquet, *Phys. Rev. Lett.*, 2006, **96**, 186102.
24 G. S. Beavers, E. M. Sparrow and R. A. Magnuson, *J. Basic Eng.*, 1970, **92**, 843–848.
25 H. M. Yeh and T. W. Cheng, *J. Membr. Sci.*, 1999, **154**, 41–51.
26 D. G. Perez, N. Ferrell, N. H. Castro and D. Hansford, *Biomed. Microdevices*, 2010, **12**, 1009–1017.
27 S. Lee, E. V. Bordatchev and M. J. F. Zeman, *J. Micromech. Microeng.*, 2008, **18**, 045011.
28 F. Niklaus, P. Enoksson, E. Klvesten and G. Stemme, *J. Micromech. Microeng.*, 2001, **11**, 100–107.
29 C. T. Pan, H. Yang, S. C. Shen, M. C. Chou and H. P. Chou, *J. Micromech. Microeng.*, 2002, **12**, 611.
30 R. Arayanarakool, S. Le Gac and A. van den Berg, *Lab Chip*, 2010, **10**, 2115–2121.
31 J. W. Kwon, H. Yu and E. S. Kim, *J. Microelectromech. Syst.*, 2005, **14**, 1399–1408.
32 C. Lee, E.-H. Yang, S. Saeidi and J. Khodadadi, *J. Microelectromech. Syst.*, 2006, **15**, 686–696.
33 F. Niklaus, H. Andersson, P. Enoksson and G. Stemme, *Sens. Actuators, A*, 2001, **92**, 235–241.
34 H. S. Noh, K. S. Moon, A. Cannon, P. J. Hesketh and C. P. Wong, *J. Micromech. Microeng.*, 2004, **14**, 625.
35 H. Wu, B. Huang and R. N. Zare, *Lab Chip*, 2005, **5**, 1393–1398.
36 P. van de Witte, P. Dijkstra, J. van den Berg and J. Feijen, *J. Membr. Sci.*, 1996, **117**, 1–31.
37 L. Vogelaar, R. Lammertink, J. Barsema, W. Nijdam, L. Bolhuis-Versteeg, C. vanRijn and M. Wessling, *Small*, 2005, **1**, 645–655.
38 *Perry's Chemical Engineers' Handbook*, ed. D. W. Green, McGrawHill, 6th edn, 1984.
39 I. Blume, P. J. F. Schwering, M. H. V. Mulder and C. A. Smolders, *J. Membr. Sci.*, 1991, **61**, 85–97.
40 B. Bhushan and Y. C. Jung, *Ultramicroscopy*, 2007, **107**, 1033–1041.
41 P. Tsai, A. M. Peters, C. Pirat, M. Wessling, R. G. H. Lammertink and D. Lohse, *Phys. Fluids*, 2009, **21**, 112002.
42 P. Tsai, R. G. H. Lammertink, M. Wessling and D. Lohse, *Phys. Rev. Lett.*, 2010, **104**, 116102.
43 F. Liu, N. A. Hashim, Y. Liu, M. M. Abed and K. Li, *J. Membr. Sci.*, 2011, **375**, 1–27.
44 P. Sukitpaneenit and T.-S. Chung, *J. Membr. Sci.*, 2009, **340**, 192–205.